Non-steady 3D dendrite tip growth under diffusive and weakly convective conditions.

W. U. Mirihanage[1], K.V. Falch[2], D. Casari[2], S. McFadden[3], D.J. Browne[4], I. Snigireva[5], A. Snigirev[6], Y.J. Li[7], R. H. Mathiesen[2]

[1] School of Materials, The University of Manchester, Manchester M13 9PL, UK.

[2] Department of Physics, Norwegian University of Science and Technology, N-7491 Trondheim, Norway.

[3] School of Computing, Engineering and Intelligent Systems, Ulster University, Londonderry BT48 7JL, UK.

[4] School of Mechanical and Materials Engineering, University College Dublin, Dublin 4, Ireland.

[5] European Synchrotron Radiation Facility, 38000 Grenoble, France.

[6] Immanuel Kant Baltic Federal University, 238300 Kaliningrad, Russia.

[7] Department of Materials Science and Engineering, Norwegian University of Science and Technology, N-7491 Trondheim, Norway.

Abstract

Three dimensional α-Al dendrite tip growth under varying solute gradients in an Al-Cu-Si alloy melt has been studied using real time synchrotron X-ray imaging and mathematical modelling. X-radiographic image sequences with high temporal and spatial resolution were processed and analysed to retrieve three-dimensional spatial details of the evolving dendrite and the solute concentration field, providing vastly improved estimates for the latter, in particular for the melt regions adjacent to the dendrite tips. Computational results obtained from an extended Horvay-Cahn dendrite tip model, capable of taking into account the effects of sample confinement, showed good agreement with the experimental data, and can be taken to verify the robustness of the 3D data extraction protocol.

1. Introduction

Over the last couple of decades, X-ray imaging has become a well-established experimental approach for in situ studies of evolving solidification microstructures [1-4]. In principle, there are two different approaches, i.e. radiography (2 spatial dimensions + time) and tomography

(3 spatial dimensions + time). Since a tomogram is a 3D image reconstructed from a set of radiography projections, typically ~1000, an obvious difference between the two is acquisition time. Radiography is therefore best suited for situations involving fast dynamics, while tomography has the advantage of capturing the full three-dimensional microstructure at the expense of an increase in exposure time. There are also other distinct differences. In radiography, the sample thickness must be matched with critical solidification parameters such as the diffusion length for the process being studied, to make sure the 2D projections are made through a single column of non-overlapping dendrites. Obviously, this results in side effects that must be ascribed to sample confinement, but, on the other hand, confinement is considered beneficial to reduce convection. In tomography, three-dimensional sample shapes can be resolved. Yet, for high resolution studies, the sample size remains small, and effects of 3D confinement may still be prominent. In most situations, convective effects would be more pronounced in tomography samples than in confined radiography cells.

Although home laboratory setups have been successfully applied in many recent radiography studies [5-8], ultimately spatiotemporal performance and high-accuracy quantitative assessment of important solidification characteristics, such as solute concentration fields in the melt, require the use of high-brilliance synchrotron radiation. For *in situ* tomography, synchrotron radiation is an exclusive requirement. Several image contrast mechanisms can be utilised, but until now almost all studies reported have been based on attenuation contrast, which in the most common range of X-ray photon energies is dominated by the photoelectric absorption cross section of core-level electrons. These cross-sections basically follows the atomic number in terms of binding (and consequentially excitation) energies. Accordingly, good transmission contrast is typically obtained alloying a highly transparent primary metal with a heavier attenuating element. Hence, density differences are prominent in most systems suitable for studies. Since synchrotron beams are highly collimated

and propagate in the plane orthogonal to gravity, it is generally not possible at synchrotron beam lines to align the radiography cells such that the projected image plane has its surface normal parallel to gravity, a configuration that has become common in home laboratory experiments [5,7]. Accordingly, convection effects tend to be present in all synchrotron imaging experiments, both in radiography and tomography, making direct comparison to modelling substantially more difficult.

When it comes to published results, there is a tendency to exaggerate the resolutions obtained in both radiography and tomography. Often, resolutions reported are the nominal values for the setup, and not the physical resolutions actually obtained in the experiment. This often leads to misinterpretations or over-optimistic analysis of the results. To illustrate the problem, one could consider a high-resolution radiography or tomography study, with a nominal pixel or voxel size of 0.5 μm, and radiography acquisition time of 5 ms, yielding one tomogram every 5^{th} second. Following the Nyquist limit, the nominal spatial resolution would be 1 μm, and the temporal resolution would be 5 ms for the radiogram and 5 s for the tomogram. If such a setup is used to study dendritic growth, and tips grow with a velocity of e.g. 10 μm/s, temporal blurring caused by the relative motion of the contrast object (here dendrite tip) with respect to the camera during exposure would result in a local spatial resolution at the tip of about 50 μm in the reconstructed tomogram, while the radiograms would image the tip in projection with a blurring effect of only 50 nm, well below the nominal resolution limit. Hence, for such a case radiography would allow for a spatiotemporally resolved study of the growth process, while tomography would not. The example also serves to illustrate another point: The physical resolution in 2 or 3D imaging of dynamical systems varies locally in the image, and is often dominated by temporal blurring effects rather than by the nominal resolution of the setup. The fact that 3D reconstructed morphologies look dendritic does not mean that they are accurate time-resolved images of the growth process. It is important to take account of these

aspects when comparing the two approaches, and in particular when deciding which method should be applied. In fact, if an alloy system and a monochromatic photon energy are chosen to yield a strong contrast between transparent crystals and an attenuating solute-enriched melt, one should expect to be able to reveal the effects of concentration gradients in the liquid when claiming to have a time-resolved image sequence of dendritic growth; such solute transport is really the controlling mechanism that restricts tip growth and determines the solid-liquid interface morphology. To our knowledge, this still has to be demonstrated successfully for *in situ* tomography studies of solidification microstructures.

In a recent study [9], we demonstrated that 3D spatial information on dendrite tips and other 3D morphological characteristics could be extracted from 2D radiographic projections under some simple and rather realistic assumptions. Thus, the work provided 4D data (3 spatial dimensions + time) of unprecedented resolution on the morphological development of columnar dendrites in an AlCuSi-alloy. In the present study, we extend the 3D rendering methodology to include also a full analysis of the Cu-enrichment in the solute. Thus, the two protocols combined provide 4D data on tip morphologies and accompanying local melt concentration fields with spatiotemporal resolutions that extend well beyond those demonstrated by in situ X-ray tomography [10-12]. To evaluate the merits of the 3D data extraction protocol, the 3D tip morphologies and solute field characteristics extracted will be compared with results calculated from a Horvay-Cahn [13] based dendrite tip model developed by McFadden and Browne [14] to handle the case of free growth under confinement, and slightly modified to adapt to the current case study with columnar dendritic growth.

2. X-ray imaging and quantitative data extraction

The experimental results have been extracted from measurements carried out at the Micro Optics Test Bench (MOTB), later extended to become the Hard X-ray Transmission Microscope (HXM) setup [15] at the ID6 beamline of the European Synchrotron Radiation Facility (ESRF). The data were collected using 14.5 keV monochromatic X-rays with full-field parallel beam imaging over 0.9 x 0.7 mm^2 field of view (FoV), acquired at 10 Hz frame rate during directional solidification parallel with gravity. The sample was a ~140 μm thick, 12 X 25 mm^2 sheet of alloy Al-15%wt.Cu-9%wt.Si-0.015%wt.Sr. The experimental conditions were controlled via a Bridgman furnace, described in detail elsewhere [16]. For the current image sequence, the imposed temperature gradient G ~ 40 K/mm, while the sample pulling velocity was ~ 10 μm/s.

In all subsequent work and analysis of the experimental data, a fixed right-handed Cartesian coordinate laboratory frame is employed, with $\hat{e}_x$ is parallel to the incident X-ray beam, whereas $\hat{e}_y \times \hat{e}_z$ (right->left, bottom->top) spans the projected image plane. The image sequence directly exhibits detailed information on the projected (y,z,t)-spatiotemporal distribution of Cu solute concentrations with the evolving dendrite tip radii, as shown in Figure 1. In a previous study of the same sequence, interdendritic solute concentration levels were quantified and extrapolated across the projected dendrites, to allow extraction of spatially resolved details also along $\hat{e}_x$ of the dendrite morphologies from X-ray attenuation contrast image processing [9]. Thus, complete (x,y,z,t) data are readily available for the dendrite tips, within the limits of experimental resolutions and errors propagating from image processing. As outlined in Figure 1, and further presented in details elsewhere [9,17], the recorded image sequence clearly displays the dynamic nature of dendritic solidification, and is strongly affected by gravity-driven flow and buoyant effects. The flow rates, as judged by the motion of connected iso-constitutional regions, appear to be relatively modest at the

macroscopic scale. At the scale of the dendrite tip, however, the flow rates reach similar magnitudes to those of the tip growth velocities. The sequence shows a macroscopic horizontally directed flow along $\hat{e}_y$, across the most permeable part of the mush, and ahead of the primary arms where it contributes to deplete accumulated solute. The FoV is a few millimetres to the left of a vertical centre line in the sample cell. Thus, the horizontal flow is assumed to arise as a consequence of natural convection in the current sample setting, presumably with an upward flow $\| \hat{e}_z$ in the sample centre region, which is deflected more or less symmetrically towards both exterior sample edges in the region where the growth front is located. The hydrodynamics are further complicated by solute plumes ejecting along - $\hat{e}_z$, out from the inter-dendritic channels of the columnar mush, and into the convective flow, causing local solute-level fluctuations ahead of the dendrite tips. With the two flow fields superimposed, the solute concentration field ahead of dendrite tips is found to vary periodically in a sinusoidal-like manner (see supplementary video 1).

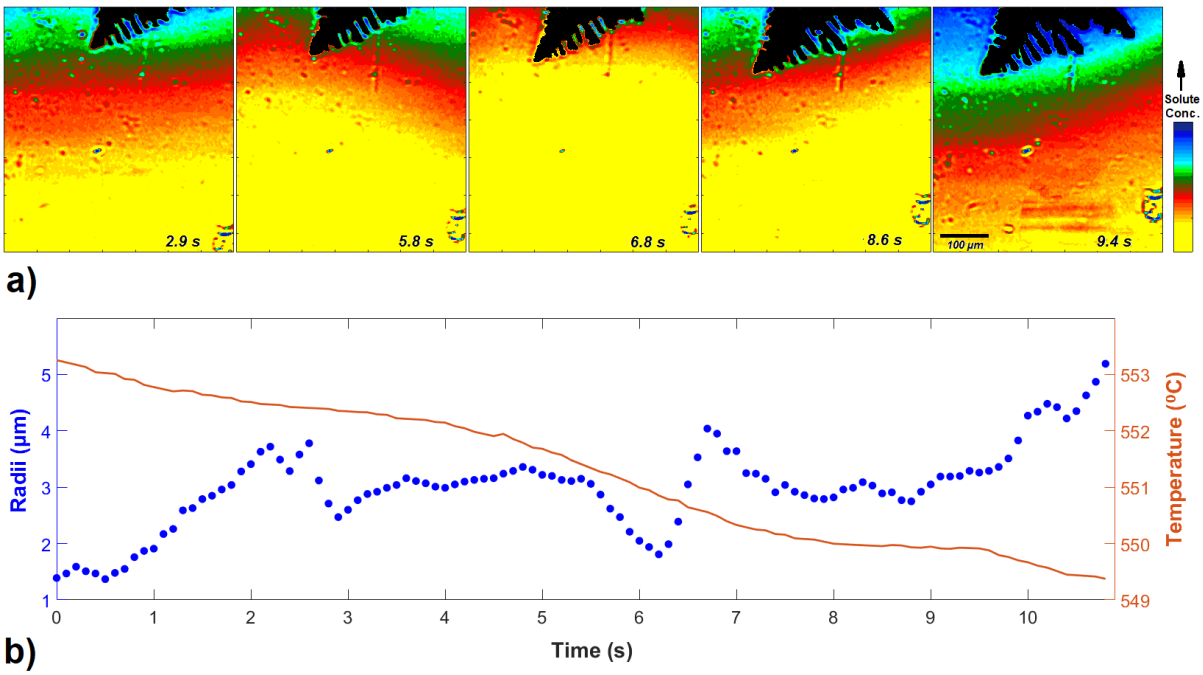

Figure 1. Evolution of a) denderite under non-steady state conditions b) extracted tip radii and tip temperature values.

In Figure 1, *G* is along - $\hat{e}_z$, parallel with gravity. However, the growth direction of the columnar dendrite(s) is inclined with respect to - $\hat{e}_z$. Thus, the inclined growth direction, combined with the melt flow, give rise to asymmetric solute gradients at the two sides of the dendrite tip, apparent in the 2D radiographic projected image plane (see Figure. 1). Along -$\hat{e}_x$, on the other hand, provided that the dendrite tip loci are nearly in middle of the cell (x=0), the solute field may be assumed to have mirror symmetry about the (y,z) plane in x=0. Thus, the current situation is somewhat more complex, but also perhaps more realistic, compared with archetype <100> dendrites having 4-fold rotational symmetric about the primary stalk. Due to the (y,z) asymmetry of the solute fields about the dendrite tip, the two sides of the tip propagate with different radii and velocities.

The dendrite tip velocity, *V*, is defined along the growth direction and a second order spline, *p* is fitted to the solid liquid interface coordinates at the dendrite tip region, extracted from the 2D images. The associated dendrite tip radius, R_{YZ}, in the projection plane is defined as $R_{YZ} = \left[\sqrt{\{1 + (p')^2\}} \right]^3 / \ | p'' |$, where *p'* and *p''* indicate the first and second derivatives of the spline fit. The dendrite tip radius orthogonal to the projected plane is denoted as R_{XZ}, and has been determined by the image processing routines outlined in ref. [9]. Figure 2 shows the basic quantities relevant to characterise the asymmetric dendrite tip, its growth and the surrounding solute field.

In comparison with the width and length of the sample, the sample thickness (136 ±10 μm) can be considered quite small. However, as dendrite tip radii are not exceeding 10 μm, it is reasonable to consider that strong confinement effects [18,19] which resemble a Hele-Shaw cell [20,21] were avoided in the experiment, particularly at the tip region. Accordingly, an effective 3D nature is present when the tip region is considered, although the tip is also clearly affected by the confinement of the crucible. From previous characterisation of thin X-radiography samples [7], it is found that columnar dendrites tend to grow in the centre of the

sample cell parallel with the crucible plates, rather than on top of or inclined to them. Thus, the confinement mainly affects the effective diffusion length along the $\hat{e}_x$-direction by hard wall blocking, and subsequent far-field pile up. In addition, the presence of a single row of columnar stalks in between planar crucible surfaces impacts the mushy zone permeability and interdendritic flow [22].

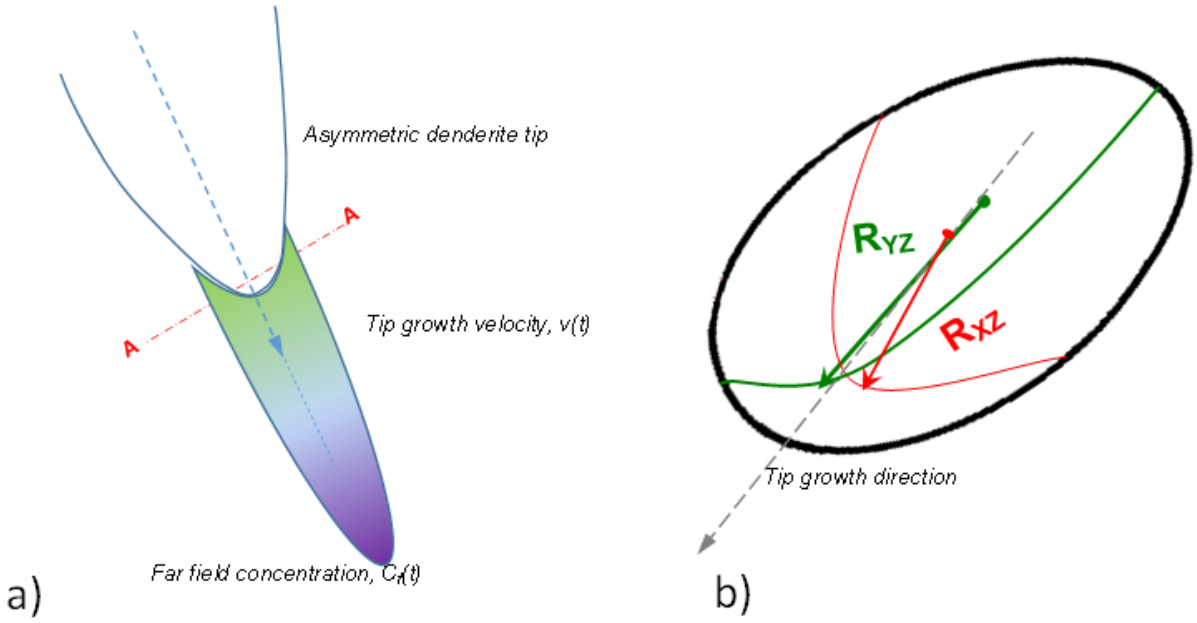

Figure 2. Identifying sketch showing the a) in-plane quantities extracted directly from the 2D projection images, and b) graphical representation of the 3D tip characteristics in terms of a thickness radius, $R_{XZ,}$ normal to the projection plane, and the in-plane radius R_{YZ}

The extraction of quantitative data for the solute concentration fields is based on X-ray attenuation contrast in the radiograms. Only the Cu enrichment is directly accessible, since the difference in attenuation between Si and Al is negligible at the given photon energy. The liquid diffusivities of Cu and Si in Al are quite similar [23,24], and to our knowledge there exist no co-diffusivities for the given conditions that should alter the balance notably [25]. It therefore seems reasonable in a first approximation to regard the X-ray attenuation contrasts to represent the micro segregation of both solute elements. Keeping in mind that α-Al growth is the

particular case studied here, it is important to take into account that the ternary alloy composition is very close to the binary Al-Si-eutectic univariant. Accordingly, Sr-modified Al-Si eutectic colonies are formed just a few Kelvins (of temperature isotherm) behind the α-Al solidification front, whereas the final Al-Cu eutectic front trails another 20 K (thermally) deeper into the mush. Thus, concerning the solute enriched interdendritic melt, more or less all of the Si of the local melt will be consumed by the eutectic reaction within 1-2 diffusion lengths from the dendrite tip, whereas most of the Cu remains in the melt. Therefore, it seems reasonable to assume that the plumes ejected out of the mush at semi regular intervals are enriched mainly in Cu, and as these plumes mix into the diffusion zone of the tip, so the dendrite tip growth in the combined diffusive-convective regime is restricted mainly by Cu-transport.

With the imposed temperature gradient and the furnace configuration, the isotherms over the field of view were assumed closely horizontal, and yielding a constant temperature field along $\hat{e}_Z$ throughout the 11 s that corresponds to the duration of the analysed sequence. Accordingly, the temperature field was extracted for all volumetric elements as $T(x, y, z) = T(z) = T_0 + G\Delta z$, with $\Delta z = z\text{-}z_0$, as the relative distance to an established reference temperature isotherm T_0 in z_0. As an example, the time series of the dendrite tip temperature and corresponding radii values are provided in Figure 1 b. Further details on the temperature field extraction can be found in ref. [9].

With the laboratory frame origin located at the dendrite tip, the accompanying concentration, $C(x,y,z)$ at distance $r=(x^2 + y^2 + z^2)^{1/2}$ from the tip is

$$C(x, y, z) = C_f + \left(C_t - C_f\right) \exp\left(-\frac{V}{D_l} r\right) \quad (1)$$

Here C_t and C_f represent solute compostion at the tip, and the far field solute compostion, respectively. V and R are the tip growth velocity and radius, respectively, while D is the solute

diffusivity in the liquid. The value, C_{pix}(y,z), for any image pixel (y, z) in the fully liquid region could be equated to an integral of eqn. (1) along $\hat{e}_x$ taken over the sample thickness, and assuming x=0 to be in the centre of the cell,

$$C_{pix}(y,z) = \frac{2}{S}\int_0^{S/2} C(x,y,z)dx. \qquad (2)$$

In the calculations employing equation (1) and (2), flow effects along $\hat{e}_x$ are assumed to be negligible. Such an assumption seems fairly reasonable taking into account the sample confinement.

2. Evolution model for the dendrite tip

The model of McFadden and Browne [14] was developed specifically to enable experimental measurements of solute concentration ahead of the dendrite tip to define the operating conditions back at the tip itself. It requires ansatz solution as a part of its mathematical framework, but a basic outline of the model can be presented through the relationship between solute concentration field, dendrite tip and growth related parameters as

$$\frac{C_t - C_f}{C_t(1-k)} = Pe^P\left(1+\frac{B}{P}\right)^{\frac{1}{2}}\left[J(P,B) - J\left(P\left(1+\frac{2\delta}{R}\right),B\right)\right], \qquad (3)$$

and solute concentraion at a given parabolic inteface cordinate, α, is

$$C_l(\alpha) = C_f + \left(C_t - C_f\right)\frac{J(P\alpha^2,B) - J(P\alpha_B^2,B)}{J(P,B) - J(P\alpha_B^2,B)}, \qquad (4)$$

where δ is the look ahead distance from the dendrite tip to the measured bulk compostion (far field distance), $P = \frac{1}{2}RVD^{-1}$ is the solute Peclet number and k is the partition coefficient. C_t

is assigned under the assumption that local equilibrium applies at the interface, employing the temperature at the given interface coordinate, and the liquidus slope of the phase digaram [14]. The integral function, *J*, is the ansatz function and is given as

$$J(\omega, B) = \int_{\omega}^{\infty} \frac{e^{-u}}{\sqrt{u\,(B+u)}}\, du, \qquad (5)$$

where *u* is an intermediate parameter in the integration process and ω is a constant. *B* is a shape factor which correlates to the 3D nature of the dendrite via the the aspect ratio of its 3D cross section. If *A* is taken as the ratio between the tip radii measured orthogonal to its center-axis, established such that $A \leq 1$, the relation between *A* and *B* is defined as

$$A^2 = (1+B)^{-1}. \qquad (6)$$

Model simulations were carried out using a Matlab-routine which basically discretises equations 3-5 to numerically predict the solute concentration profiles ahead of the dendrite tip, with the far-field location fixed. For the computations, 3D dendritic tip parameters (the radii and parameter *A*), tip velocity, far-field concentration data and calibrated temperature field data were used as input for each frame. With such additional experimental data available, the iterative computational procedures outlined in ref. [14] were simplified. The values, k = 0.14 and D = 3.9 x 10^{-9} m^2/s were used for the computations [23].

4. Results and Discussion

One of the main novel outcomes of the present study is that it allows extraction of experimental data on the evolution of the dendrite tip morphology and solute concentration fields in 3D. The procedure facilities a full 3D profile rendering of the dendrite tip for each frame, accompanied

with the detailed solute concentration of the liquid at any given spatial coordinate within the limits of our voxel size of approximately 0.3 μm^3. A few example illustrations of such details are presented in Figure 3.

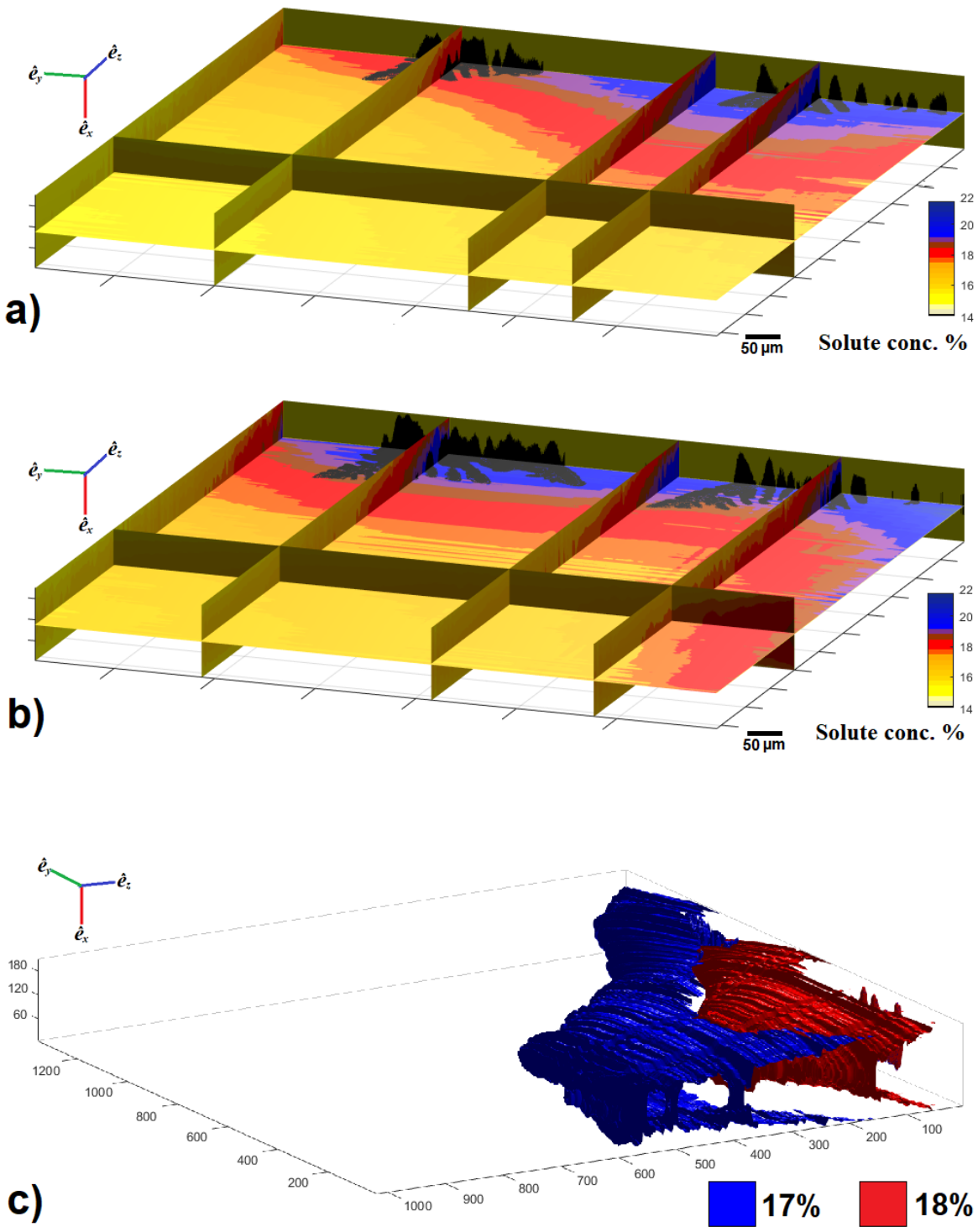

Figure 3. 3D slice profiles of concentration variations in different planes at solidification times a) t = 5.0 s b) t= 11.0 s. c) Iso-concentration surface at 17% wt. Cu and 18% wt. Cu at t=5.0 s. Here in fig. c, axis dimensions are given in voxels of 0.65 x 0.65 x 0.65 µm^3.

Using the dendrite tip evolution model and the mathematical procedure outlined in ref. [14], including equations (3) and (4) given here, the liquid concentration profile ahead of the dendrite tip can be calculated, provided that C_f is known, and P and B have been assigned values. Experimentally, $C_{pix}(y,z)$ values are extracted from all frames of the image sequence, allowing for model-independent values of $C(x,y,z)$, including C_t, to be computed via the analysis outlined in eqns. (1) and (2). Thus, detailed and complete comparisons can be made

quite readily between model predictions and experimental data. For this purpose, concentration values for a given set of coordinates along the tip growth direction have been extracted from the measured data, and compared directly with model predictions, as illustrated in Figure 4.

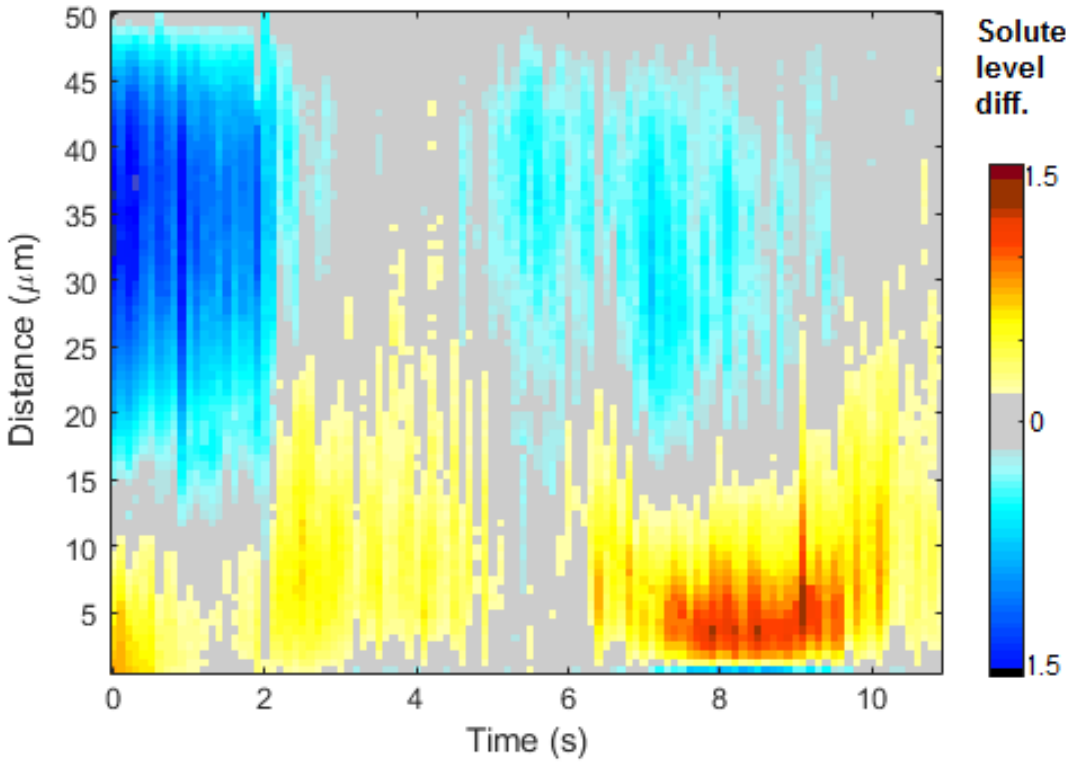

Figure 4. Difference between solute concentrations from model predictions and experimental estimates, as a function of time and distance from the tip along its growth direction (displayed difference = model values - experimental values). Solute concentration differences for the scale bar are in %wt. Cu.

As shown in Figure 4, model predictions are in reasonable agreement with values 3 and 5extracted from experimental data. The most pronounced deviations, around solidification times t ~ 0.5 s and t ~ 8.0 s, correspond to situations that can be ascribed to more pronounced flow-driven mass transport around the dendrite tip.

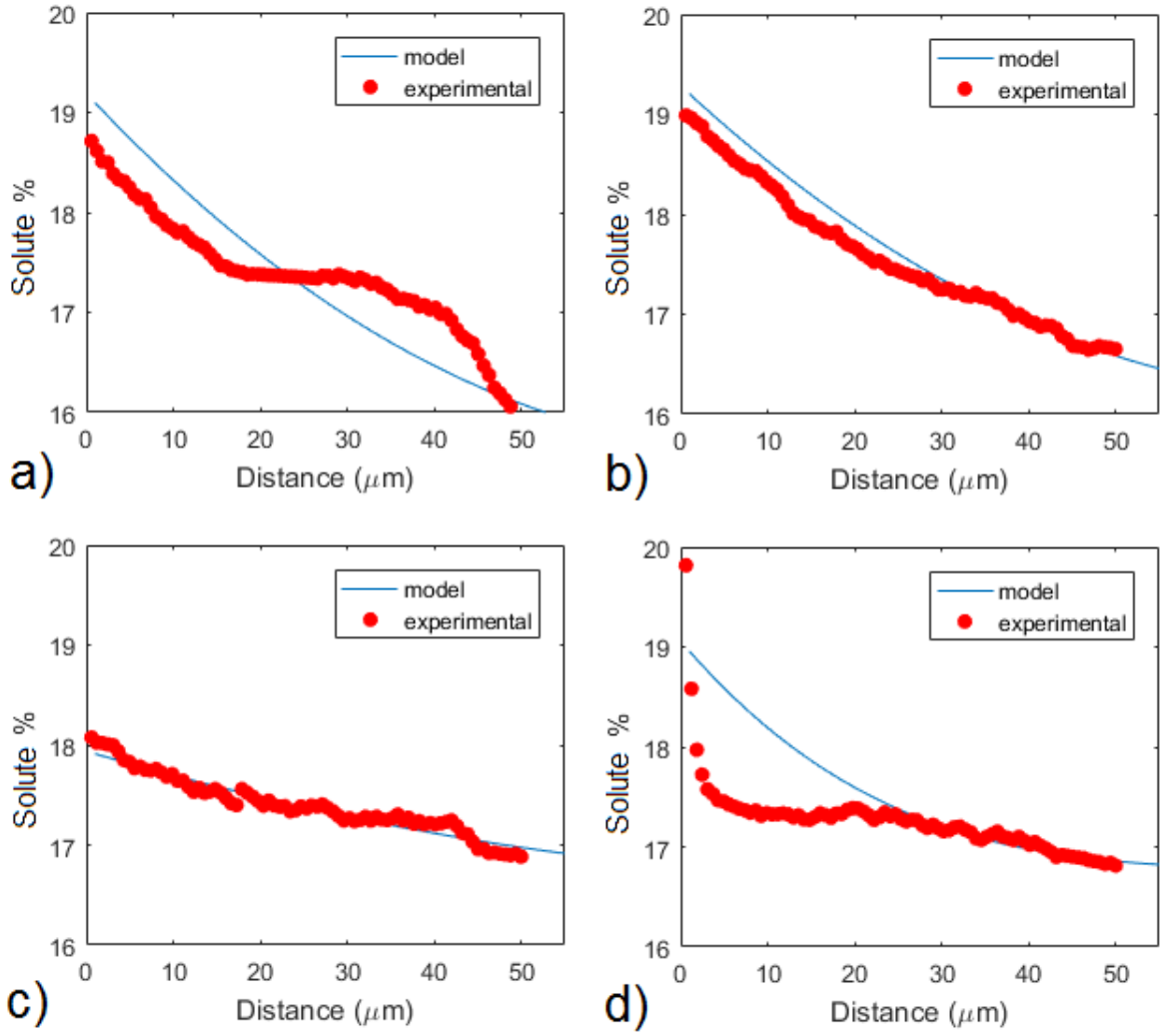

Figure 5. Comparison of model predicted and experimentally obtained solute profiles along the primary tip growth direction for solidification times a) t = 0.7 s, b) t = 2.1 s, c) t = 5.4 s, d) t = 8.4 s. The solute concentration values of the scale bars are in % wt. Cu.

The differences between predicted and experimentally obtained solute concentration values, along the growth direction are further illustrated in Figure 5. Particularly, Figure 5.a and 5.d show strong discrepancy in solute concentration profiles between model and experiment at t = 0.7 s and 8.4 s, respectively. Figure 5.a shows a situation where solute

concentration far ahead of the tip enriches rather abruptly by the combined effect of a solute plume ejection from a neighbouring columnar channel, and the macroscale convective flow. In Figure 5.d, a short diffusion length is apparent with a very steep solute gradient close to the tip just after the macroscale convective flow has swept away the solute enriched field ahead of the tip.

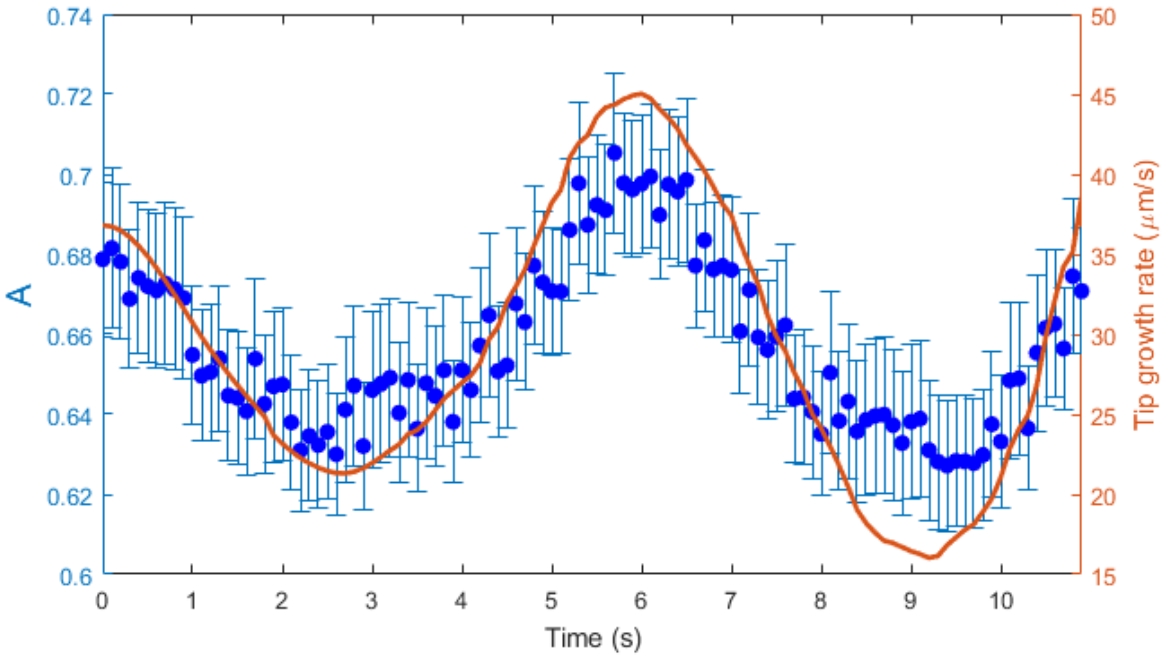

Figure 6. Time evolution of tip aspect ratio, *A* for radii along orthogonal planes for the 3D dendrite(●). The errors bars represent the errors that can be associated with 3D computation. Line plot (y-scale on right side) indicates the tip growth rate along the growth direction.

Differences in solute concentration levels at the two opposite sides of the dendrite tip with a non-axisymmetric dendrite evolution in (y,z) plane were observed in this experiment [9,17]. A common converged tip radius for each frame was obtained via employing a cubic spline fit to the extracted interfacial coordinates and the tip radii data were directly fed into the model [14], which considers a single dendrite tip radius in one 2D plane, together with its 3D

characteristics defined through the parameter *A*. As shown in Figure 6, with varying tip growth rate, the aspect ratio of the dendrite in-plane to out of plane radii is found to vary marginally with solidification time. The fluctuations are modest at a maximum amplitude of 5%. The nature of the tip 3D aspect ratio undulations is observed to be directly proportional to the growth rate of the dendrite tip (as shown in the supplementary video).

As shown here, flow within the diffusion zone of the dendrite tip is critical to the solute profile and consequently to the characteristics of the evolving tips, such as *V* and *R*. Such fluctuating growth conditions may become particularly pronounced when flow rates are comparable with tip growth velocities. For example, the condition illustrated in Figure 5.d as well as in other experimental and modelling works [26-28], deviate markedly from the steady state symmetric dendrite tip, even under purely diffusive conditions. Such scenarios represent situations which cannot be handled properly by the model unless hydrodynamics are incorporated. Overall, the predictive power of the model seems promising, although data extracts of a similar quality taken under less convective conditions would be required for more detailed assessment. In fact, it is however clear that the data extraction protocol established for X-radiography herein and in the preceding study [8] can provide detailed and unprecedented 4D data for validation of or comparison to dendritic growth models.

5. Summary

Data on dendrite tip curvatures and accompanying solute concentration fields have been extracted in 4D applying a novel image processing algorithm to a sequence of synchrotron radiograms collected in situ during directional solidification of AlCuSi. The data extraction procedure has been validated by a comparison with dendrite tip characteristics and solute diffusion fields calculated using an extension of the Horvay-Cahn model. With directional solidification parallel with gravity and an enhanced density for solute-enriched liquid,

conditions a for steady-state columnar growth cannot be reached in the experiments, and from the radiographic image sequence, and accompanying video, the presence of both macro- and meso-scale hydrodynamics are evident. Yet, as the local melt flow in the vicinity of dendrite tips was moderate and varied semi-periodically with a low frequency, it was possible to find relatively long periods of duration where the 3D tip growth characteristics and solute field extracted from the experiment compare well with values computed by the purely diffusive model. The good agreement between model predicted values and data extracted from the experiment is taken as evidence that the scheme proposed for 4D data extraction is sound and reasonably robust.

Acknowledgements

The European Synchrotron Radiation Facility is acknowledged for granting access to beamtime. Parts of the work leading to these results has been carried out under project ExoMet under the European Community's Seventh Framework Programme, contract FP7-NMP3-LA-2012-280421, EPSRC(UK) grant EP/P02680X/1 and project no. 218404/F50 granted by the Norwegian Research Council under the SYNKNOYT programme.

References

1. H. Nguyen-Thi, L. Salvo, R.H Mathiesen, L. Arnberg, B. Billia, M. Suery, G. Reinhart, On the interest of synchrotron X-ray imaging for the study of solidification in metallic alloys, Compt. Rend. Phys. 13 (2012) 237-245
2. S. Akamatsu, H. Nguyen-Thi, In situ observation of solidification patterns in diffusive conditions, Acta Mater. 108 (2016) 325-346
3. R. H. Mathiesen, L. Arnberg, H. Nguyen-Thi, B. Billia, In situ x-ray video microscopy as a tool in solidification science, JOM 64 (2012) 76-82
4. M. Suery, S. Terzi, B. Mireux, L. Salvo, J. Adrien, E. Marie, Fast in situ x-ray microtomography observations of solidification and semisolid deformation of Al-Cu alloys, JOM 64 (2012) 83-88

5. A.G. Murphy, D.J. Browne, W.U. Mirihanage, R.H. Mathiesen, Combined in situ X-ray radiographic observations and post-solidification metallographic characterisation of eutectic transformations in Al-Cu alloy systems, Acta Mater. 61 (2013) 4559-4571
6. H. Nguyen-Thi, G. ReinhartG. Salloum-Abou-JaoudeD. J. BrowneA. G. MurphyY. HoultzJ. LiD. VossA. Verga, R. H. MathiesenG. Zimmermann, XRMON-GF experiments devoted to the in situ X-ray radiographic observation of growth process in microgravity conditions, Micrograv. Sci. Techn. 26, (2014) 37-50
7. A.G. Murphy, W.U. Mirihanage, D.J. Browne, R.H. Mathiesen, Equiaxed dendritic solidification and grain refiner potency characterised through in situ X-radiography, Acta Mater. 95 (2015) 83-89
8. Y.J Xu, D. Casari, R. H. Mathiesen, Y.J. Li, Revealing the heterogeneous nucleation behavior of equiaxed grains of inoculated Al alloys during directional solidification, Acta Mater. 149 (2018) 312-325
9. W.U. Mirihanage, K.V. Falch, A. Snigirev, Y. Li, L. Arnberg, R.H. Mathiesen, Retrieval of three-dimensional spatial information from fast in situ two-dimensional synchrotron radiography of solidification microstructure evolution Acta Mater. (2014) 241-247
10. J. W. Gibbs, K. A. Mohan, E. B. Gulsoy, A. J. Shahani, X. Xiao, C. A. Bouman, M. De Graef, P. W. Voorhees, The Three-Dimensional Morphology of Growing Dendrites, Scientific Reports 5(2015) 11824
11. B.Cai, J. Wang, A. Kao, K. Pericleous, A.B. Phillion, R.C. Atwood, P.D. Lee, 4D synchrotron X-ray tomographic quantification of the transition from cellular to dendrite growth during directional solidification, Acta Mater. 117(2016) 160-169
12. R. Daudin, S. Terzi, P. Lhuisseier, J. Tamaya, M. Scheel, N. Hari Babu, D.G. Eskin, L. Salvo, Particle-induced morphological modification of Al alloy equiaxed dendrites revealed by sub-second in situ microtomography, Acta Mater 125(2017) 303-310
13. G. Horvay, J.W. Cahn, Dendritic and spheroidal growth, Acta Metall. 9 (1961) 695-705
14. S. McFadden, D.J. Browne, A generalised version of an Ivantsov-based dendrite growth model incorporating a facility for solute measurement ahead of the tip, Comp. Mater. Sci. 55 (2012) 245–254
15. A. Bosak, I. Snigireva, K.S. Napolskii, A.Snigirev, High-resolution transmission X-ray microscopy: A new tool for mesoscopic materials, Adv. Mater. 22 (2010) 3256-3259
16. R H. Mathiesen, L. Arnberg, K. Ramsoskar, T. Weitkamp, C. Rau, A. Snigirev, Time-resolved X-ray imaging of aluminum alloy solidification processes, Metall. Mater. Trans. B 33 (2002) 613-623

17. W.U. Mirihanage, L. Arnberg, R.H. Mathiesen, In-situ observation of transient columnar dendrite growth in the presence of thermo-solutal convection, IOP Conf. Series: Mater. Sci. Eng. 33(2012) 012033
18. H. Emmerich, D. Schleussner, T. Ihle, K. Kassner, Confinement effects in dendritic growth, J. Phys.: Condens. Matter 11 (1999) 8981–8993
19. B. P. Athreya , J. A. Dantzig , S. Liu, R. Trivedi, On the role of confinement on solidification in pure materials and binary alloys, Philosophical Mag. 86(2006) 3739-3756
20. H.S. Hele-Shaw, The Flow of Water, Nature 58 (1898) 34-36
21. J.V. Maher, Development of viscous fingering patterns, Phys. Rev. Lett. 54 (1985) 1498-1501
22. R.H. Mathiesen, L. Arnberg, -ray radiography observations of columnar dendritic growth and constitutional undercooling in an Al-30wt%Cu alloy, Acta Mater. 53 (2005) 947-956
23. W. Kurz, D.J. Fisher, Fundamentals of Solidification, Trans Tech Publications (1992)
24. W. B. Alexander, L. M. Sifkin, Diffusion of Solutes in Aluminum and Dilute Aluminum Alloys, Physical Review B 1(1970) 3274- 3282
25. X. Yan, S. Chen, F. Xie, Y.A. Chang, Acta Mater. 50 (2002) 2199–2207
26. I. Steinbach, Phase-field models in materials science, Modelling Simul. Mater. Sci. Eng. 17 (2009) 073001
27. I. Steinbach, Effect of interface anisotropy on spacing selection in constrained dendrite growth, Acta Mater. 56 (2008) 4965-4971
28. P. Delaleau, C. Beckermann, R.H. Mathiesen, L. Arnberg, Mesoscopic simulation of dendritic growth observed in X-ray video microscopy during directional solidification of Al-Cu alloys, ISIJ International 50(2010) 1886-1894